Generation and Screening of Antigen-Specific Nanobodies from Mammalian Cells Expressing the BCR Repertoire Library Using Droplet-Based Microfluidics

Menghua Lyu,[∇] Xuyang Shi,[∇] Xiaopan Liu,[∇] Yang Liu, Xijun Zhu, Lijuan Liao, Hongyan Zhao, Na Sun, Shiyu Wang, Linzhe Chen, Linyuan Fan, Qumiao Xu, Qianqian Zhu, Kai Gao, Huaying Chen, Yonggang Zhu, Zida Li, Weijin Guo, Yue Zheng, Ying Gu, Longqi Liu,* Meiniang Wang,* and Ya Liu*
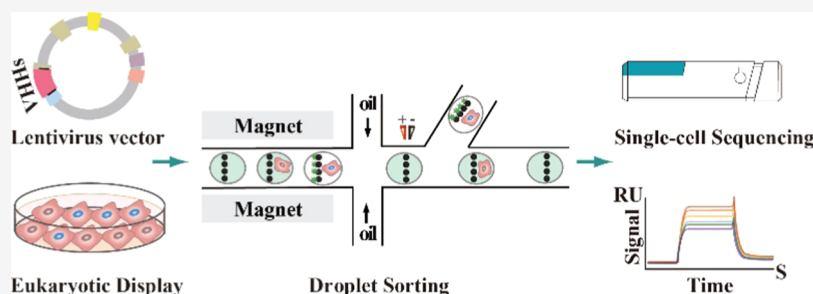
ACCESS | Metrics & More | Article Recommendations | Supporting Information

ABSTRACT: Nanobodies, also known as VHHs, originate from the serum of Camelidae. Nanobodies have considerable advantages over conventional antibodies, including smaller size, more modifiable, and deeper tissue penetration, making them promising tools for immunotherapy and antibody-drug development. A high-throughput nanobody screening platform is critical to the rapid development of nanobodies. To date, droplet-based microfluidic systems have exhibited improved performance compared to the traditional phage display technology in terms of time and throughput. In realistic situations, however, it is difficult to directly apply the technology to the screening of nanobodies. Requirements of plasma cell enrichment and high cell viability, as well as a lack of related commercial reagents, are leading causes for impeding the development of novel methods. We overcame these obstacles by constructing a eukaryotic display system that secretes nanobodies utilizing homologous recombination and eukaryotic transformation technologies, and the significant advantages are that it is independent of primary cell viability and it does not require plasma cell enrichment in advance. Next, a signal capture system of "SA-beads + Biotin-antigen + nanobody-6 × His + fluorescence-labeled anti-6 × His (secondary antibody)" was designed for precise localization of the eukaryotic-expressed nanobodies in a droplet. Based on this innovation, we screened 293T cells expressing anti-PD-L1 nanobodies with a high positive rate of targeted cells (up to 99.8%). Then, single-cell transcriptomic profiling uncovered the intercellular heterogeneity and BCR sequence of target cells at a single-cell level. The complete complementarity determining region (CDR3) structure was obtained, which was totally consistent with the BCR reference. This study expanded the linkage between microfluidic technology and nanobody applications and also showed potential to accelerate the rapid transformation of nanobodies in the large-scale market.

■ INTRODUCTION

Nanobody, also known as VHH, is a variable domain of the heavy chain of naturally occurring heavy-chain IgG antibodies originating from the serum of *Camelidae* (such as alpaca, llama, camel, etc.).[1] This structure allows nanobodies to confer a light molecular weight (12−15 kDa) but still retains a high binding affinity to a specific antigen, although it is smaller than conventional antibodies (150 kDa).[2,3] They exhibit unique properties including low immunogenicity,[4] high stability,[5,6] strong affinity, wide modifiability, deep tissue penetration, and so on.[7] Benefiting from these inherent favorable features, nanobodies have proven to be promising tools for immunotherapy and antibody-drug development, such as

biomedical applications in tumor diagnosis and therapeutics, imaging-guided surgery,[8] delivery of chemotherapeutic drugs, and more.[2,4] To date, several nanobody-drugs have been developed and approved by the FDA, revealing favorable effectiveness in inhibiting cancer cell growth.[9,10]
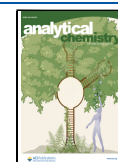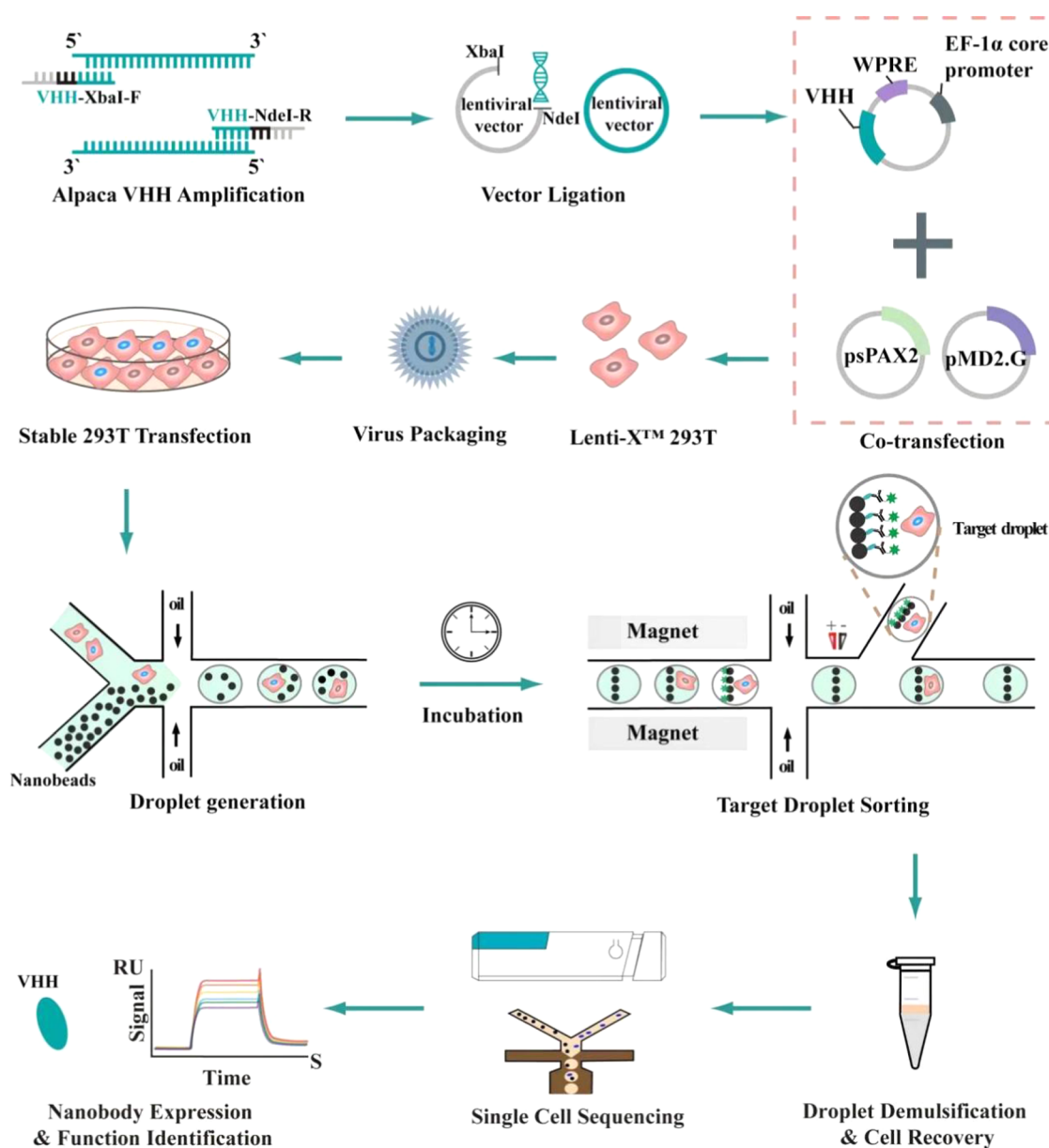
Figure 1. Experimental workflow of the platform for the generation and screening of PD-L1-specific nanobodies from 293T cells expressing the BCR repertoire library for cancer immunotherapy. Main steps included VHH-PD-L1 DNA sequence amplification, vector ligation, cotransfection, virus packaging, stable 293T transfection, target droplet sorting, VHH DNA synthesis, nanobody expression, and function identification.

With the increasing importance of nanobodies, some techniques have been adapted for screening. For example, phage display technology is one of the oldest and most mature methods that is simple in operation and has been broadly promoted.[11,12] In practice, it identifies antigen-specific nanobodies within four weeks after 3−5 rounds of panning, and the success rate of identifying nanobodies from an immune library is close to 100%.[12] However, phage belongs to the prokaryotic expression system, and due to the lack of proper protein processing, the selection procedure may suffer from non-specific bindings and insufficient modifications.[12,13] Thus, a clear drawback in this manner may be the low antibody affinity occasionally. In contrast, the yeast display system has the advantage of being compatible with fluorescence-activated cell sorting (FACS) and posttranslational modification machinery,[11,14] but it is limited by the library size of 10^7 diverse capacity[12] and intense background noise of FACS, eventually

resulting in false positives.[14,15] Beyond that, the two technologies mentioned above are based on the simple binding of nanobodies displayed on the membrane with an antigen rather than depending on a binding function directly, which is more accurate and direct.

To bridge the demand gap between the nanobody market and disadvantages of the existing methods, it is critical to build a high-throughput nanobody screening platform to cater to the increasing trend of nanobodies. To date, droplet microfluidics has exhibited improved performance in high-throughput and rapid screening for traditional antibodies. In 2020, Gérard et al. presented a droplet microfluidic system, *Celli GO*, for IgG-secreting primary cell screening to characterize antibody binding to soluble and membrane-bound antigens. The key to the design of sorting is the wrapping of plasma cells and signal detection reagents (including magnetic beads, antigens, and fluorescent dye conjugated secondary antibodies) in

microdroplets, which offers an intuitive way to visualize plasma cell-secreting antigen-specific antibodies. The platform successfully sorted droplets at up to 600/s and screened antigen-specific IgGs with high affinity from mice plasma cells.[16]

However, the application of similar approaches in the screening of nanobodies also directly requires cell viability, quantity, etc., which has caused a lot of barriers. In the work of *Celli Go*, immune cells were collected from the lymph nodes/thymus of antigen-immunized mice and enriched for plasma cells with a commercial kit before enveloping them into droplets. Here, the high viability of plasma cells should guarantee enough antibody secretion, and the sufficient sensitivity of the detection reagents allows for distinguishing the signals from antigen-specific antibodies. For the study of antigen-specific nanobodies, camels (such as alpaca, American Camel, humped camel, etc.) are typically used as experimental subjects, and intravenous blood collection is performed after 3−5 rounds of immunization (usually 50−100 mL).[11] In general, the proportion of circulating plasma cells in peripheral blood is relatively low compared with that of the thymus, and it is essential to enrich plasma cells before sorting or run multiple rounds of the screening process to obtain a high positive rate.[17] However, there is still a lack of commercial reagents available for alpaca plasma cell enrichment. In addition, multiple rounds of screening may affect the viability of primary B cells, thus reducing the final efficiency. Furthermore, commercial anti-Alpaca IgG secondary antibodies are polyclonal antibodies with a low binding sensitivity, which in turn makes the research much more challenging.

In this study, we combined the eukaryotic display system with microfluidic devices to adapt the nanobody screening (Figure 1). In brief, a eukaryotic gene expression program was built with homologous recombination and eukaryotic transformation technologies, which substituted for enriching plasma cells from *Camelidae* PBMCs. Then, a signal capture system, "SA-beads + Biotin-antigen + nanobody-6 × His + fluorescence-labeled secondary antibody (fluorescence-labeled anti-6 × His)", was employed to sensitively capture the eukaryotic-expressed nanobodies in a droplet. We cloned a gene fragment of anti-PD-L1 through the polymerase chain reaction (PCR) with a pair of primers (VHH-*Xba*I-F; VHH-*Nde*I-R), and the VHH gene fragments were assembled to the restriction endonuclease linearized lentiviral vector by homologous recombination. The recombined lentiviral vector and packaged plasmids (psPAX2 and pMD2.G) were cotransfected into Lenti-X 293T cells for virus packaging and concentration. Then the concentrated lentivirus were used to transfect with 293T cells for nanobody secretion. Microfluidic chips of droplet generation and cell sorting were adopted to scan the signal expression and location of targets. Finally, single-cell RNA sequencing of DNBelab C4 greatly facilitated the acquirement of the target gene and opened up the possibility of fast acquisition of the gene segment when extracting the primary cells. Our platform greatly expands the important application of microfluidic technology in nanobody production and provides a universality reference for the development of novel functional antibodies, which facilitates the resolution of efficiency and throughput challenges when dealing with infectious disease screening and other assay discoveries.

■ MATERIALS AND METHODS

Reagents. The full list of reagents (Table S1) and equipment information (Table S3) is provided as supplementary material.

Microfluidic Chip Design and Fabrication. Two separate types of droplet-based microfluidic chips were designed in our work: (Figure S2A,B) droplet generating chip and (Figure S2E) droplet sorting chip. The droplet generating chips were provided by HiComp Microtech (Suzhou) Co., Ltd. The diameters of the oil phase, the cell phase, and the outlet in droplet generation chips were 10, 5, and 1.5 mm, respectively. More detailed information on channel dimensions and the chip manipulation principle has been provided in Figure S2. For the fabrication of the droplet sorting chip, a mask was designed using computer-aided design (CAD) software and microfluidic channels were patterned onto silicon wafers with SU-8 photolithography. Subsequently, all chips were fabricated using poly(dimethylsiloxane) (PDMS) and then bonded onto a glass slide using oxygen plasma (Harrick plasma cleaner, PDC-002). For more details on the microfluidic chip, please refer to our previous research.[18]

VHH-Lentivirus Library Construction. The empty lentiviral vector pLV-EF1α was linearized with the endonucleases *Xba*I and *Nde*I. VHH-6 × His genes were then ligated into the linearized lentiviral vector using homologous recombinase. The recombinant product (pLV-EF1α-VHH-6 × His) was subsequently transformed into the DH5α-competent *Escherichia coli* cells through chemical transformation. The transformed *E. coli* cells were screened with ampicillin (Amp).[19] The pLV-EF1α-VHH-6 × His plasmid was then extracted using an endotoxin-free plasmid extracting kit.

Lentivirus Preparation and Virus Titration. 293Lenti-X cells were transfected with the target plasmid pLV-EF1α-VHH-6 × His and the packaging plasmids, using a transfection reagent (ethyleneimine polymer solution mixed with Opti-MEM), when the cell confluence reached 80%. The medium was replaced with a fresh complete culture medium 6 hours after transfection. After 48 hours, the lentivirus-containing supernatant was harvested and filtered through a 0.45 μm filter membrane to remove cell debris. The lentivirus was concentrated by centrifuging at 45,000 rpm for 90 mins at 4 °C. Then, the concentrated lentivirus was aliquoted with a T009 serum-free medium and stored at −80 °C.

To test lentivirus titers, series of volumes (i.e., 0, 0.04, 0.2, 1, 5 μL) of concentrated lentivirus supernatants were used to infect each of the 200,000 Jurkat cells. After 72 h of infection, the Jurkat cells were harvested and stained with 1 μL of the PE-labeled Hamster Anti-Mouse TCR β chain. Subsequently, the stained Jurkat cells were subjected to flow cytometry analysis. As the mouse TCRβ sequence was designed in our lentivirus vector, TCR β positive means that these Jurkat cells were infected. The obtained data were processed with FlowJo v10.0.7. Samples were analyzed in duplicates if not indicated otherwise. The functional lentiviral titer, given in transducing units (TUs) per ml, was calculated according to the following formula[20]

$$\text{infectious titer} = \frac{200000 \cdot P}{V} \cdot 10^3$$

where 200,000 is the number of cells at the time of transduction, P is the percentage of TCR β-positive cells, and V is the volume (in μL) used for transduction.

Construction of a Stable Cell Line and Cell Culture. To obtain the 293T-VHH-6 × His stable cell line, 293T cells were infected using lentivirus transfection, which integrated VHH-PD-L1 DNA into the genome with multiplicity of infection (MOI) = 1. The infected cells were cultured in DMEM medium supplemented with 10% FBS and a 1% Penicillin-Streptomycin solution. The supernatant of infected cells was collected for anti-PD-L1 nanobody purification and testing.

Purification of Eukaryotic-Expressed Anti-PD-L1 Protein. The expression supernatant was collected by centrifugation at 12,000g for 20 min and was filtered through 0.22 μm syringe filters. Immobilized metal-ion affinity chromatography (IMAC) was performed using a HisTrap FF 1 mL column and an AKTA-Pure purification system (GE Healthcare) following the instruction manual. The histidine-tagged PD-L1 nanobody was eluted with 200 mM imidazole/phosphate-buffered saline (PBS). Next, the purity of the eluted protein was checked by SDS-PAGE and ultrafilter by Amicon Ultra 3 kDa centrifugal filters to exchange the buffer with PBS.

Specific ELISA Binding Assay. Specific ELISA binding was carried out to evaluate the antigen binding specificity of the PD-L1 nanobody. The testing antigens, such as PD-L1-FC, PD-1-FC, B7-1-FC, B7-2-FC, CTLA-4-FC, and BSA, were coated onto a 96-well ELISA plate at 1 $\mu g/mL$ in 100 mM NaHCO$_3$ overnight at 4 °C separately. The plate was blocked with 2% bovine serum albumin (BSA) in 0.05% PBST (phosphate-buffered saline solution with a low-concentration detergent solution) at room temperature for 2 h. Then, 100 μL of the PD-L1 nanobody dilution at 1.5 $\mu g/mL$ was coincubated at 37 °C with all of the antigen-coated wells for 2 h. After 5 rounds of washes with 0.05% PBST, a 2500-fold diluted HRP-conjugated 6 × His-tag antibody was added and incubated at room temperature for 1 h. Following final washes, 100 μL of TMB solution was further incubated for 10 min in the dark, and the reaction was then stopped by adding an equal volume of the TMB STOP solution. The absorption at 450 nm was read on a plate reader within 30 min.

Binding Ability Evaluation. A total of 1 $\mu g/mL$ PD-L1-Fc protein was coated onto a 96-well ELSA plate overnight at 4 °C. After being blocked with 2% BSA at room temperature for 2 h, a series of 4-fold PD-L1 nanobody dilutions with a starting concentration of 0.6 $\mu g/mL$ (~40 nM) were added and incubated at room temperature for 1 h. Next, the plate was washed with 0.05% PBST 5 times followed by maintaining with an HRP-conjugated 6 × His-tag antibody (1:2500 in 1% BSA/PBST) for another 1 h. After 5 times of washing, 100 μL of TMB solution was added and incubated out of light for 5 min, followed by an equal volume of the TMB STOP solution. The absorption at 450 nm was measured on a plate reader, and the EC50 binding curve was performed using GraphPad Prism 8.0 software.

Surface Plasmon Resonance (SPR). Surface plasmon resonance in this study was employed to measure the nanobody affinities. Briefly, Fc-fusion PD-L1 protein was captured by a Series S Sensor Chip Protein G that resulted in an SPR response of about 239 RU. A series of dilutions (10, 5, 2.5, 1.25, 0.625, 0.3125, and 0.15625 nM) of the PD-L1 nanobody were injected with HBS-P+ running buffer at a flow rate of 30 $\mu L/min$ for 120 s, followed by 180 s of dissociation.

The sensor chip surface was regenerated after each injection with 10 mM Glycine-HCl (PH 1.5) at a flow rate of 30 $\mu L/min$ for 20 s. The kinetic was analyzed using BIAcore T200 evaluation with the 1:1 binding model.

Flow Cytometry Analysis. Tumor A375 cells over-expressing the PD-L1 protein on the cell membrane, A375-PD-L1, were adopted to further evaluate the binding function of the eukaryotic expression anti-PD-L1 nanobody. A375-PD-L1 cells were first incubated with the anti-PD-L1 nanobody (eukaryotic or prokaryotic expression) and then stained with anti-6 × His-AF 647. The A375-PD-L1 cells stained with the commercial reagent anti-CD274-APC served as the positive group, and the control group was set to merely incubate with anti-6 × His-AF 647 (see Methods for detailed descriptions). The binding efficiency of the anti-PD-L1 nanobody was defined as the percentage of AF 647-positive cells using flow cytometry.

Working Buffer Preparation. Working buffer for droplet generation consisted of DMEM/F12 added to 0.1% Pluronic F68, 25 mM HEPES pH 7.4, 5% fetal bovine serum with ultralow IgG, 1% Pen/Strep, and 6% Ficoll.

Bead Preparation. Streptavidin-coated paramagnetic nanoparticles were incubated with biotin-antigen (beads: biotin-PD-L1 = 1 mg: 21 μg) for 15−30 min with PBS containing 0.1% PF68 at room temperature. The beads were then washed with PBS containing 0.1% PF68 three times to remove the free biotin-PD-L1. In the final step, beads were diluted with a working buffer containing 100 nM Alexa Fluor 488 coupled 6 × His Tag monoclonal antibody to a concentration of 1 mg/mL.

Droplet Generation, Collection, and Incubation. Droplets were generated based on the negative pressure system with two aqueous phases and an oil phase, where biotin-antigen coupled SA-beads and FITC coupled secondary antibody resuspended with a working buffer were referred as aqueous phase 1 and the cell suspension was prepared as aqueous phase 2. In the operation stage, droplet generation oil (200 μL), aqueous phase 1 (50 μL), and phase 2 (50 μL) were added into the corresponding reservoirs of the chip, and −30 kPa of negative pressure was applied on the chip to supply the driving force for droplet generation (Figure S2A,C,D). In phase 1, the final concentration of SA-beads was 1 mg/mL; during this process, a higher concentration of SA-beads can potentially clog the droplet generation chip. Conversely, a lower concentration of SA-beads will reduce the signal-to-noise ratio in the droplet and affect the judgment of targets. In phase 2, the cell density of 1 × 10^7 cells/mL was set to maximize the single-cell encapsulation rate.[21] After encapsulation, all droplets were collected into 2 ml collection tubes and cultured in an incubator set to 37 °C, 5% CO$_2$, with a humidity of 95% for 2 h.

Microfluidic Droplet Sorting and Recovery. After incubation, we injected the droplets into the sorting chip at rates of 20 $\mu L/h$ (droplet) and 800 $\mu L/h$ (oil) with two droplet syringe pumps, making the droplets pass through the sorting junction at 100 Hz. A 488 nm laser with a power of 10 mW excited the fluorescence of droplets flowing through "position A" of the sorting junction (Figure S2E). The specific technical details in Figure S3 are described next. The photomultiplier tube (PMT) with a gain of 0.47 detects the fluorescence signal of the droplets, converts the optical signals into electrical signals, and then transmits the electrical signals to a voltage comparator and a single-chip microcomputer. The
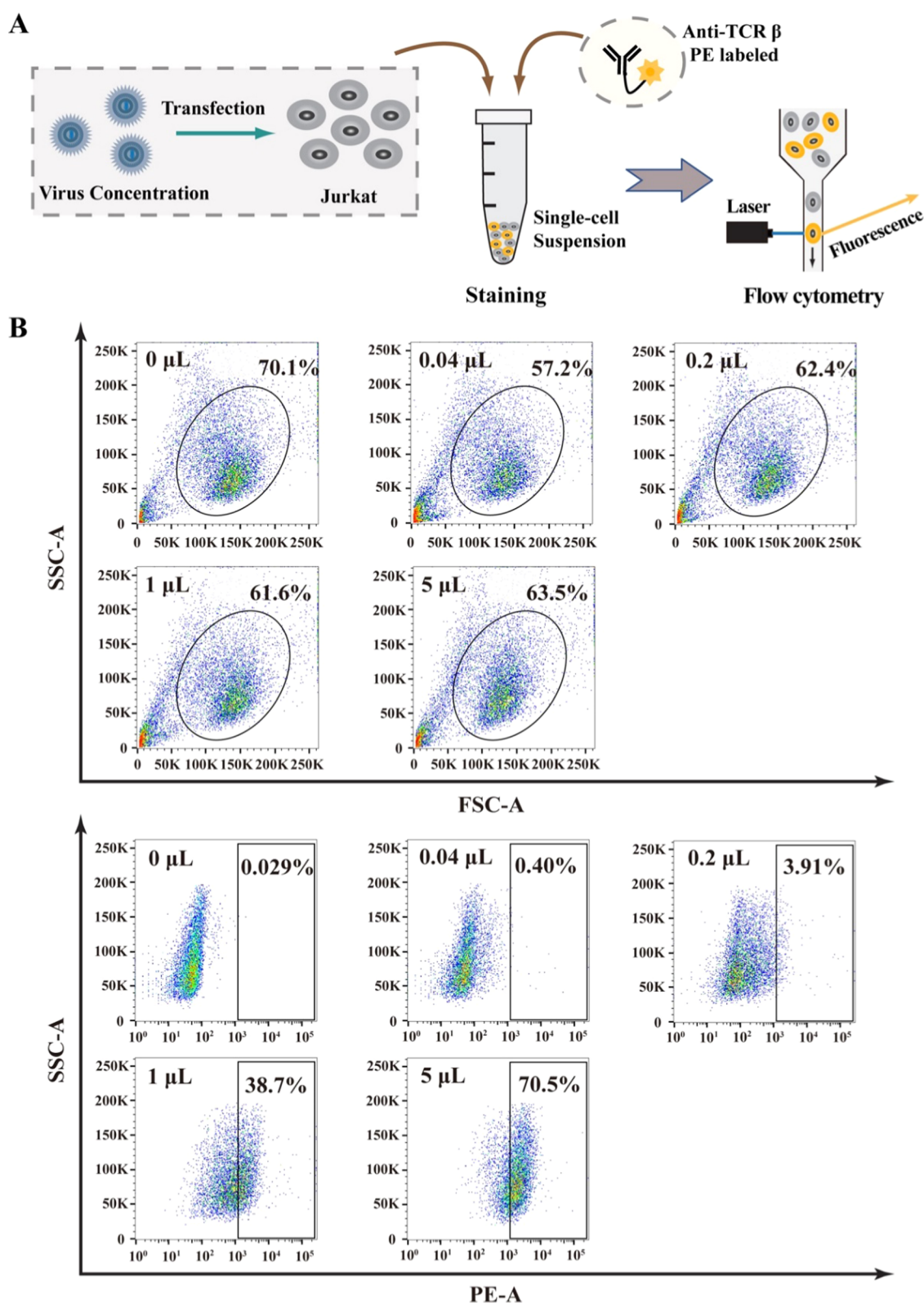
Figure 2. Titration of the concentrated lentivirus using Jurkat cells. (A) Experimental workflow of lentivirus titration. Step 1: A series of volumes (0, 0.04, 0.2, 1, and 5 μL) of concentrated lentiviruses are used to transfect 20,000 Jurkat cells. Step 2: After 72 h of infection, 10,000 Jurkat cells from each group are subjected to stain with 1 μL of PE-labeled anti-TCR β. Step 3: Five stained samples are analyzed by flow cytometry to infer the lentivirus titer. (B) Flow cytometric analysis of different groups. Cells in similar states are selected for statistics of the proportion of infected cells, and the sample transfected with 0 μL of lentivirus is regarded as the negative control.

voltage comparator judges the appearance and disappearance of each droplet from the received electrical signal and sends the

corresponding logical value (true or false) to the single-chip microcomputer. The single-chip microcomputer integrates and
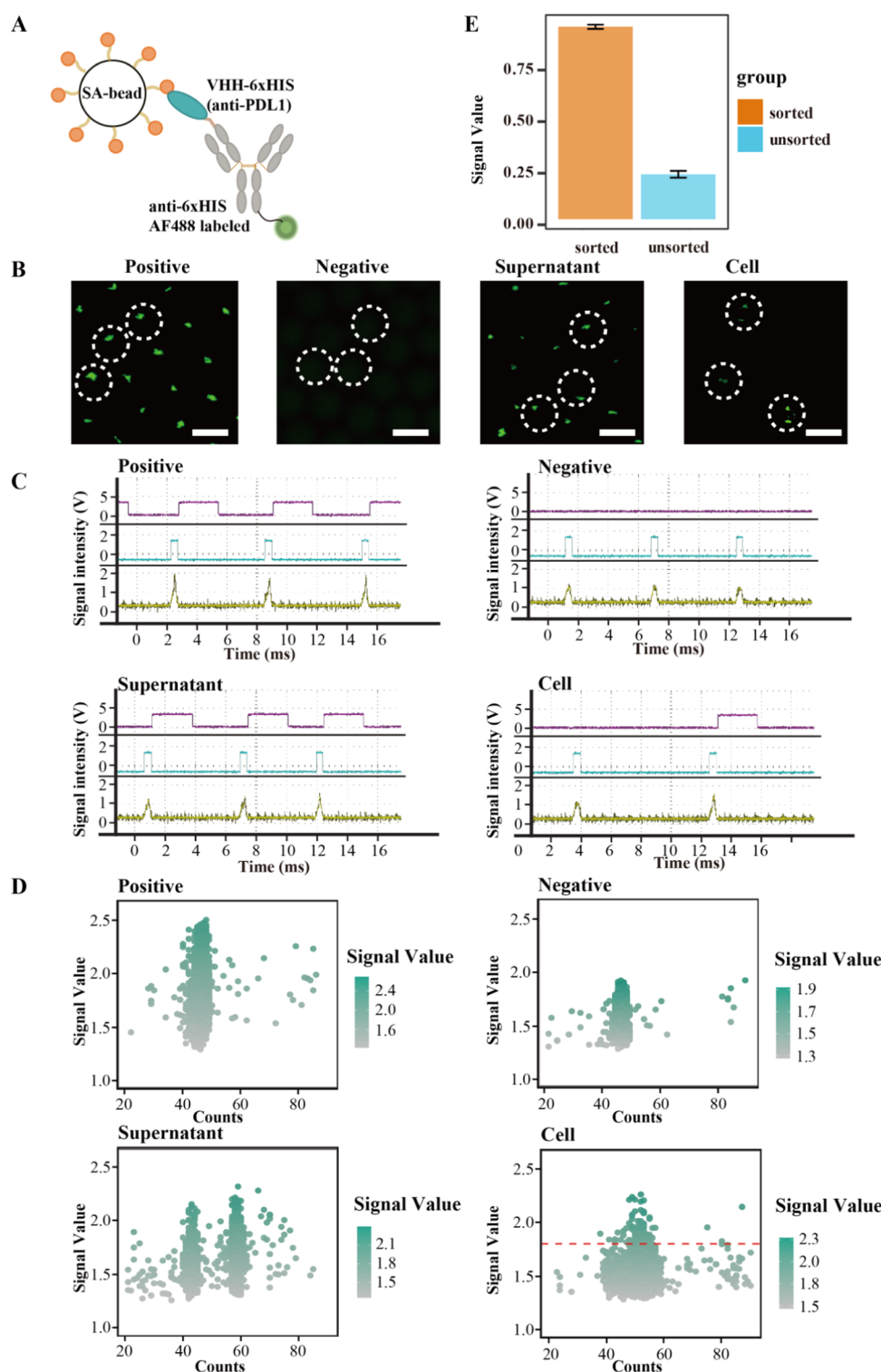
Figure 3. Screening of nanobody-secreting cells in the microfluidic system. (A) Design of the signal acquisition on magnetic beads. (B) Fluorescence microscopy images and (C) wave recoding of the four samples (Positive, Negative, Supernatant, Cell). Scale bar is 50 μm. (D) Scatter plot of signal analysis results. The red line represents the sorting threshold for the positive rate. (E) Comparison of the positive rate before and after sorting.

calculates data from the PMT and the voltage comparator. When the logical value from the voltage comparator is "true" and the ratio of the maximum value to the mean value from the PMT is larger than the threshold, the single-chip microcomputer sends a deflection signal; otherwise, it will not work. The deflection voltage is a square wave of 20 kHz, 600 Vpp.

Two 1.5 ml EP tubes were used to collect the positive droplets (target) and negative droplets (waste) downstream of the sorting junction. After that, the target droplets were broken by adding 100 μL of a DMEM culture medium mixed with 100 μL of 1H,1H,2H,2H-perfluoro-1-octanol and then centrifuged at 400g for 5 min.
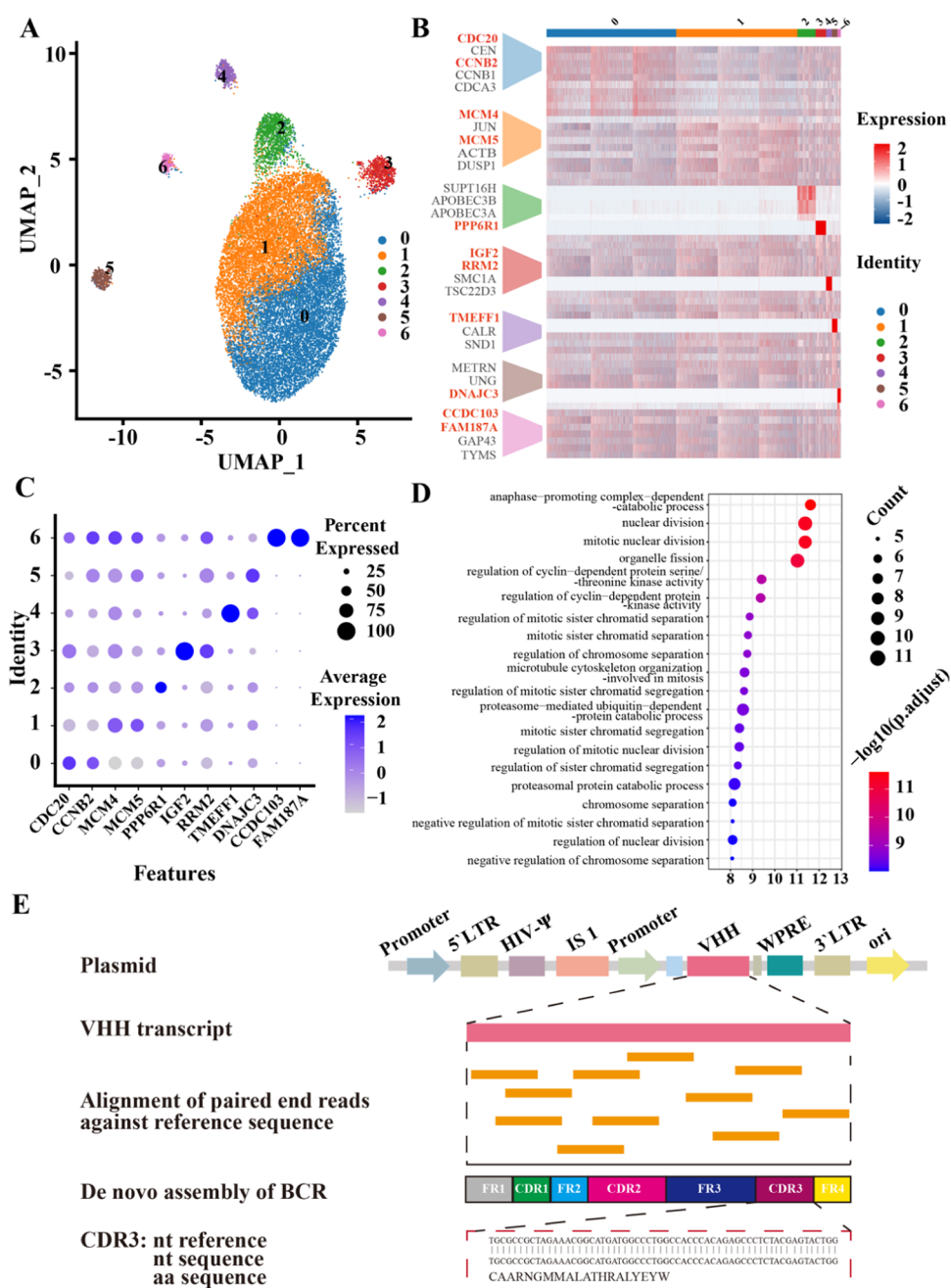
Figure 4. Unveil targeted 293T cell phenotypes and the BCR sequence with scRNA-seq data. (A) UMAP showing all single-cell patterns in a two-dimensional space. (B) Heatmap of top 10 differentially expressed genes (DEGs) in each subset. (C) Dotplot of marker genes in each cluster. (D) GO analysis based on DEGs of cluster 0. (E) Workflow for BCR sequence identification.

Construction of the Sequencing Library and Single-Cell Sequencing. We performed the single-cell library construction by choosing the DNBelab C4 technology. Briefly, single-cell suspensions underwent a series of steps including droplet generation, emulsion breakage, bead collection, reverse transcription, and cDNA amplification to generate libraries. Next, the libraries were quantified by the Qubit ssDNA assay kit, and the sequencing was performed on the ultrahigh-throughput DIPSEQ T1 sequencer.

Single-Cell Data Analysis. The FASTQ data of single-cell transcriptome and the BCR sequence were processed by the PISA pipeline (version 1.10.2) (https://github.com/shiquan/

PISA). For the analysis of single-cell transcriptomes, a standard format of the gene expression matrix was generated with reference to the GRCh38 human genome for downstream analysis. The gene expression matrix was processed using Seurat (version 4.0.1).[22] Cells were filtered based on the distribution of genes and the unique molecular identifier (UMI). Cells expressing less than 400 genes or higher than 4500 genes were removed, and mitochondrion DNA less than 10% were retained. Filtered data were normalized and scaled by Seurat "NormalizeData" and "ScaleData" functions with default parameters. The top 30 PCs were summarized to construct an SNN graph and FindClusters with Louvain

algorithms following the standard Seurat pipeline. Then, we conducted dimension reduction and illustration of cells in a two-dimensional space with UMAP. The raw FASTQ files of the BCR data set were processed by the PISA pipeline (version 1.10.2) (https://github.com/shiquan/PISA), and the target BCR sequence was then identified by TRUST4.[23]

■ RESULTS AND DISCUSSION

Lentivirus Packaging and 293T Cell Transfection. The diagram of the recombinant vector designed for eukaryotic expression is shown in Figure S1. The lentivirus vector containing the HIV packaging RNA sequence (HIV-Ψ), the transposable element IS1, the EF1α core eukaryotic promoter element, and the membrane-localized mouse TCRβ sequence was taken as the backbone. The anti-PD-L1 nanobody VHH sequence with a secretory signal peptide (SP) on its 5′ ends and 6 × His Tag on 3′ ends was inserted between 5′-long terminal repeats (5′ LTR) and 3′-long terminal repeats (3′ TLR) of the lentivirus vector. The SP ensured the correct secretion of nanobodies in eukaryotic cells, and the 6 × His Tag enabled purification and functional detection of the eukaryotic-expressed anti-PD-L1 protein. Given that the EF1α has been used as the eukaryotic promoter of the recombinant vector and the corresponding inserted gene sequence, the recombinant vector was named "pLV-EF1α-VHH-6 × His." In Figure 2A, each group of the 200,000 Jurkat cells was infected with 0 μl (negative control), 0.04, 0.2, 1, and 5 μL of the concentrated virus, separately. After infection, Jurkat cells were subjected to stain with the anti-TCRβ-FITC and subsequently analyzed by flow cytometry. The results in Figure 2B displayed the proportion of infected cells in each group detected by flow cytometry. With the FSC and SSC parameters, we selected cells from each group in a similar state for further analysis, and these selected cells accounted for 70.1, 57.2, 62.4, 61.6, and 63.5% of the total. Data indicated that only 0.029% of Jurkat cells that were TCRβ-FITC-positive were found in the negative control (0 μL virus). However, TCRβ-FITC-positive Jurkat cells represented 0.40, 3.91, 38.7, and 70.5% in other experimental groups of the virus infection with different volumes (0.04, 0.2, 1, and 5 μL). Finally, we calculated that the virus titer was in the range of 2×10^7 to 7.74×10^7 TU/mL.

Virus Transfection and Detection of the Positive Rate. The 293T cells were subjected to VHH-lentivirus infection with multiplicity of infection (MOI) = 1, and the positive rate of infected cells was then counted based on the anti-PD-L1 expression by 293T cells after about 96 h of transfection. Supporting Table shows that ∼62.56% of the 293T cells were transfected (named anti-PD-L1−293T).

Selection of PD-L1 Antigen-Specific Nanobody-Secreting Cells. We designed a nanobody capture system in a droplet consisting primarily of streptavidin-coupled magnetic beads with a diameter of 300 nm, biotinylated PD-L1 (antigen), and AF488-labeled anti-6 × His. In this system, binding of the antigen to magnetic beads was mediated by biotin−streptavidin interaction; the anti-PD-L1 nanobody can specifically bind to the antigen and the AF488-labeled anti-6 × His was finally conjected with the 6 × HIS Tag (Figure 3A). Subsequently, the fluorescence of AF488-labeled anti-6 × His was enriched on the surface of beads. At that point, substantial reduction of the fluorescent secondary antibody in the droplet occurred, thereby contributing to the waveform in Figure 3C when the target cell was identified in the signal capture system. In contrast, anti-6 × His cannot be indirectly bound with the

magnetic beads in the absence of antigen-specific antibodies, but can be evenly distributed in the droplet. The waveform result in Figure 3C reflects the procedure described above; the purple line represents the single-chip microcomputer signal, the blue line represents the voltage comparator signal, and the yellow line represents the photomultiplier tube (PMT) signal. We set four experimental groups (Positive, Negative, Supernatant, Cell), and fluorescence and bright microscopy images of these are presented in Figures 3B and S5. Of these, we observed a similar phenomenon in both the positive control and the supernatant, which is the green fluorescence signal enriched near the bead line, but it was hardly detectable in the negative group. It also indicated that the nanobody in cell supernatants was PD-L1-specific. Statistically, the positive rate of cells was 62.56% (Figure 3C), which was consistent with Supporting Table 2. Samples in these four groups were separately passed through the signal collection system of microfluidics, and the corresponding patterns obtained are outlined in Figure 3D. In this step, we set the threshold for the compromise between the positive rate and the cell recovery rate. In other words, once we expect a higher positive rate, the recovery rate will decrease. The positive rate of unsorted cells was 26.5%, while after sorting based on our system, the positive rate of cells reached 99.8% (Figures 3E and S4), which revealed the high efficiency of our screening system.

Single-Cell RNA Sequencing. To identify the transcriptome characteristic and BCR sequence of the isolated targeted 293T cells, we performed single-cell sequencing based on the DNBelab C4 to achieve heterogeneity analysis of 293T cells. After stringent quality control and filtering with multiple criteria (see Methods), transcriptome data from 19,172 single 293T cells were acquired. For cell clustering, 293T cells were assigned to different clusters with no apparent bias as shown in the UMAP plot of Figure 4A, and the top 10 feature genes of each cluster through DEG analysis are presented in a heatmap (Figure 4B). Interestingly, according to the results of DEG and GO analyses, we could propose that various cluster cells may be at different phases of the cell cycle. For example, the genes *CDC20* and *CCNB2* were highly expressed by cluster 0, and these genes exhibited a stronger enrichment in pathways such as nuclear division and regulation of sister chromatid segregation, indicating that cluster 0 may be at the mitosis anaphase and telophase (Figure 4C), and the GO analysis further confirmed this result (Figure 4D). Clusters 1, 2, 3, and 4 were related to DNA replication and DNA cytosine deamination, which demonstrated that these cells were in the G1/S phase of the mitotic cell cycle (Figure S7A−D). The DEGs in cluster 5 were associated with the protein kinase regulator activity, which was also involved in the S phase of the mitotic relevant process (Figure S7E). The result of GO analysis in cluster 6 revealed that the DEGs were related to the nuclear envelope disassembly and membrane disassembly, and cluster 6 may be associated with the mitosis telophase (Figure S7F). Furthermore, we amplified the VHH regions of the nanobody using custom primers to identify the BCR sequence of the single 293T cell, and its pattern was identified as indicated in Figure S6. The raw data was calculated by the PISA program, and the full length of the VHH sequence was then assembled from short-read data with the aid of TRUST4.[23] Thus, we were able to obtain a complete complementarity determining region (CDR3) structure, which was totally consistent with the BCR reference (Figure 4D). All present results suggested that our approach was
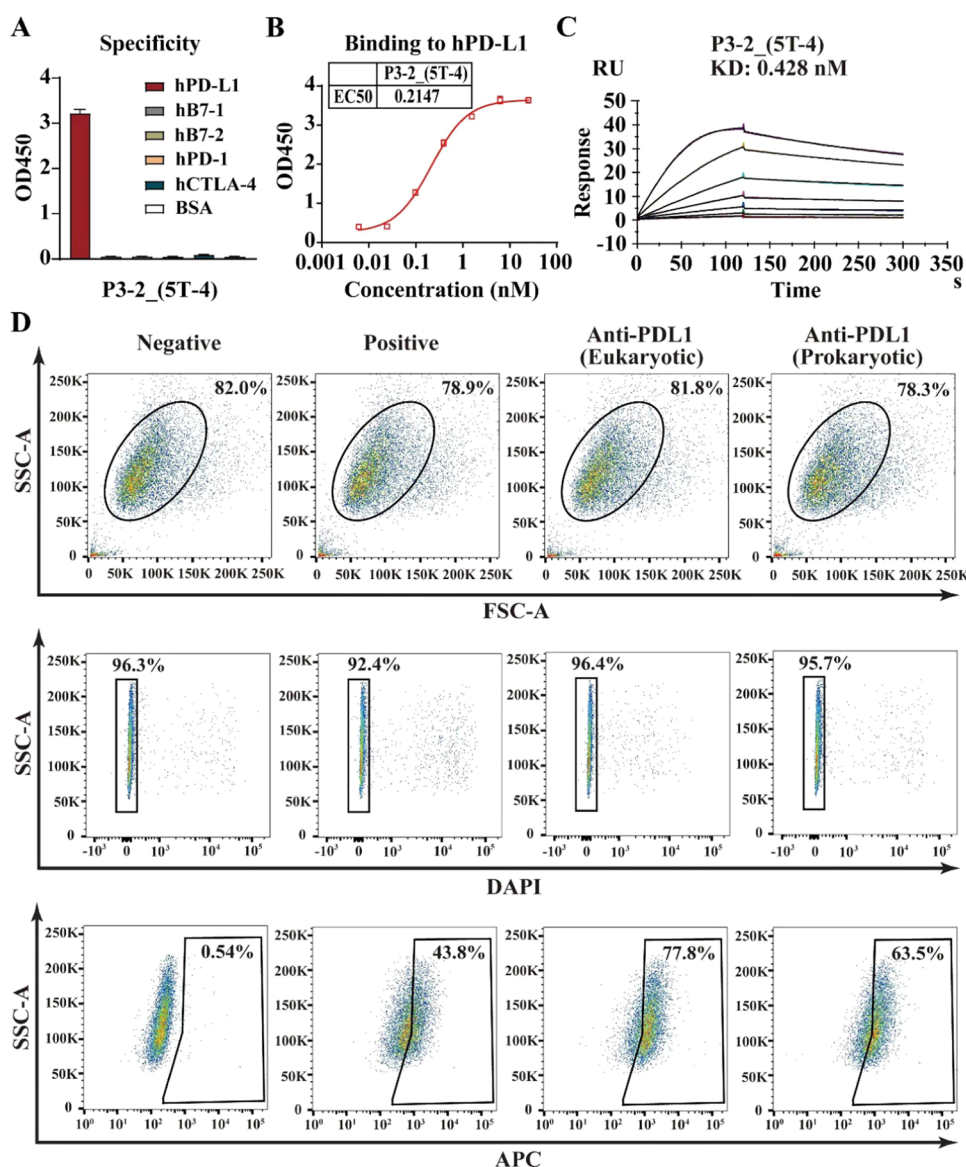
Figure 5. Functional verification of the anti-PD-L1 nanobody secreted from the 293T cell. (A) ELISA testing for antigen-specificity of the anti-PD-L1 nanobody. (B) EC50 of anti-PD-L1 with PD-L1 testing by ELISA. (C) Dynamic parameter of the anti-PD-L1 nanobody detected by SPR. (D) Functional testing of the anti-PD-L1 nanobody with flow cytometry.

sufficient to simultaneously identify the intercellular heterogeneity and predict the BCR sequence of target cells, which was more meaningful to the primary B cell samples. Previously reported studies depending on droplet-based microfluidics to screen target cells mainly concentrated on the cell function. For a deeper mechanism study, single-cell omics provides us an opportunity to identify the intercellular heterogeneity of primary cells and also explains the reasons for the functional differences at the molecular level.

Functional Verification of the Anti-PD-L1 Nanobody. Based on the result of Figure 5, we concluded that the purified PD-L1 nanobody can specifically bind to PD-L1, while a similar behavior was not observed in some other B7 family members such as human B7-1, B7-2, CTLA-4, and PD-1 (Figure 5A). Besides, the nanobody exhibited a high affinity to human PD-L1 at the subnanomolar level (EC50 = 0.2147 nM, KD value = 0.428 nM; Figure 5B).

Overexpressed PD-L1 proteins on the cell membrane of A375 cells and A375-PD-L1 were further examined to evaluate the binding function of the eukaryotic-expressed anti-PD-L1 nanobody. The binding efficiency of the anti-PD-L1 nanobody was evaluated by the percentage of APC+ cells analyzed with flow cytometry (Figure 5D). With the FSC-A/SSC-A parameter, cells in a similar state were selected. Living cells were further marked with DAPI-gate, and the cell viability was greater than 92% in each group. FACS analysis of these living cells showed that the percentage of PD-L1+ cells (APC+) in the negative control was 0.54%, and those in the positive control, the anti-PD-L1 nanobody (eukaryotic), and the anti-PD-L1 nanobody (prokaryotic) were 43.8, 77.8, and 63.5%, respectively. These data also indicated that the binding function of eukaryotic-expressed anti-PD-L1 was comparable to that of the commercial reagent.

■ CONCLUSIONS

Here, we developed an effective strategy to screen the secreted nanobodies specific for the PD-L1 antigen through homologous recombination and mammalian cell engineering using

high-throughput microfluidics and identified their biological function at the single-cell level. Meanwhile, it provides us with a reliable scheme that bypasses some limiting factors of insufficient samples and primary cell viability. With the capability of high-throughput screening and combined with single-cell omics, it may revolutionize next-generation cancer immunotherapy and drug development as well as advance basic research involving functional characteristics of the cell.

■ ASSOCIATED CONTENT

ⓈⒾ Supporting Information

The Supporting Information is available free of charge at https://pubs.acs.org/doi/10.1021/acs.analchem.2c00865.

> Vector map of the recombinant lentivirus; and analysis of the BCR sequence pattern using an Agilent 2100 bioanalyzer (PDF)

■ AUTHOR INFORMATION

Corresponding Authors

Longqi Liu − *BGI-Shenzhen, Shenzhen 518083, China*; Email: liulongqi@genomics.cn

Meiniang Wang − *BGI-Shenzhen, Shenzhen 518083, China*; Email: wangmeiniang@genomics.cn

Ya Liu − *BGI-Shenzhen, Shenzhen 518083, China; Shenzhen Key Laboratory of Single-Cell Omics, BGI-Shenzhen, Shenzhen 518100, China*; ⓞ orcid.org/0000-0002-3936-1685; Email: liuya1@genomics.cn

Authors

Menghua Lyu − *BGI-Shenzhen, Shenzhen 518083, China; College of Life Sciences, University of Chinese Academy of Sciences, Beijing 100049, China*

Xuyang Shi − *BGI-Shenzhen, Shenzhen 518083, China; College of Life Sciences, University of Chinese Academy of Sciences, Beijing 100049, China*

Xiaopan Liu − *BGI-Shenzhen, Shenzhen 518083, China*

Yang Liu − *BGI-Shenzhen, Shenzhen 518083, China*

Xijun Zhu − *BGI-Shenzhen, Shenzhen 518083, China*

Lijuan Liao − *BGI-Shenzhen, Shenzhen 518083, China*

Hongyan Zhao − *BGI-Shenzhen, Shenzhen 518083, China*

Na Sun − *BGI-Shenzhen, Shenzhen 518083, China*

Shiyu Wang − *BGI-Shenzhen, Shenzhen 518083, China*; ⓞ orcid.org/0000-0001-8851-1697

Linzhe Chen − *Department of Biomedical Engineering, School of Medicine, Shenzhen University, Shenzhen 518060, China*

Linyuan Fan − *BGI-Shenzhen, Shenzhen 518083, China; College of Life Sciences, University of Chinese Academy of Sciences, Beijing 100049, China*

Qumiao Xu − *BGI-Shenzhen, Shenzhen 518083, China*

Qianqian Zhu − *BGI-Shenzhen, Shenzhen 518083, China*

Kai Gao − *BGI-Shenzhen, Shenzhen 518083, China*

Huaying Chen − *School of Mechanical Engineering and Automation, Harbin Institute of Technology, Shenzhen, Shenzhen 518055, China*; ⓞ orcid.org/0000-0003-1054-4362

Yonggang Zhu − *School of Mechanical Engineering and Automation, Harbin Institute of Technology, Shenzhen, Shenzhen 518055, China*

Zida Li − *Department of Biomedical Engineering, School of Medicine, Shenzhen University, Shenzhen 518060, China*; ⓞ orcid.org/0000-0002-1353-9414

Weijin Guo − *Department of Biomedical Engineering, Shantou University, Shantou 515063, China*

Yue Zheng − *BGI-Shenzhen, Shenzhen 518083, China*

Ying Gu − *BGI-Shenzhen, Shenzhen 518083, China*

Complete contact information is available at:
https://pubs.acs.org/10.1021/acs.analchem.2c00865

Author Contributions

∇M.L., X.S., and X.L. contributed equally to this work.

Notes

The authors declare no competing financial interest.
The data relating to this study are available in the CNGB Nucleotide Sequence Archive (CNSA: https://db.cngb.org/cnsa; accession number CNP0002667).

■ ACKNOWLEDGMENTS

■ REFERENCES

(1) Hamers-Casterman, C.; Atarhouch, T.; Muyldermans, S.; Robinson, G.; Hammers, C.; Songa, E. B.; Bendahman, N.; Hammers, R. *Nature* **1993**, *363*, 446−448.

(2) Leslie, M. *Science* **2018**, *360*, 594−597.

(3) Muyldermans, S. *Annu. Rev. Biochem.* **2013**, *82*, 775−797.

(4) Asaadi, Y.; Jouneghani, F. F.; Janani, S.; Rahbarizadeh, F. *Biomarker Res.* **2021**, *9*, No. 87.

(5) Turner, K. B.; Zabetakis, D.; Goldman, E. R.; Anderson, G. P. *Protein Eng., Des. Sel.* **2014**, *27*, 89−95.

(6) Dumoulin, M.; Conrath, K.; Van Meirhaeghe, A.; Meersman, F.; Heremans, K.; Frenken, L. G. J.; Muyldermans, S.; Wyns, L.; Matagne, A. *Protein Sci.* **2009**, *11*, 500−515.

(7) Yu, S.; Xiong, G.; Zhao, S.; Tang, Y.; Tang, H.; Wang, K.; Liu, H.; Lan, K.; Bi, X.; Duan, S. *Int. J. Mol. Med.* **2020**, *47*, 444−454.

(8) Bao, G.; Tang, M.; Zhao, J.; Zhu, X. *EJNMMI Res.* **2021**, *11*, No. 6.

(9) Hargadon, K. M.; Johnson, C. E.; Williams, C. J. *Int. Immunopharmacol.* **2018**, *62*, 29−39.

(10) Darvin, P.; Toor, S. M.; Sasidharan Nair, V.; Elkord, E. *Exp. Mol. Med.* **2018**, *50*, 1−11.

(11) Muyldermans, S. *FEBS J.* **2021**, *288*, 2084−2102.

(12) Rahbarnia, L.; Farajnia, S.; Babaei, H.; Majidi, J.; Veisi, K.; Ahmadzadeh, V.; Akbari, B. *J. Drug Targeting* **2017**, *25*, 216−224.

(13) Yang, Z.; Wan, Y.; Tao, P.; Qiang, M.; Dong, X.; Lin, C.-W.; Yang, G.; Zheng, T.; Lerner, R. A. *Proc. Natl. Acad. Sci. U.S.A.* **2019**, *116*, 14971−14978.

(14) McMahon, C.; Baier, A. S.; Pascolutti, R.; Wegrecki, M.; Zheng, S.; Ong, J. X.; Erlandson, S. C.; Hilger, D.; Rasmussen, S. G. F.; Ring, A. M.; Manglik, A.; Kruse, A. C. *Nat. Struct. Mol. Biol.* **2018**, *25*, 289−296.

(15) Uchański, T.; Zögg, T.; Yin, J.; Yuan, D.; Wohlkönig, A.; Fischer, B.; Rosenbaum, D. M.; Kobilka, B. K.; Pardon, E.; Steyaert, J. *Sci. Rep.* **2019**, *9*, No. 382.

(16) Gérard, A.; Woolfe, A.; Mottet, G.; Reichen, M.; Castrillon, C.; Menrath, V.; Ellouze, S.; Poitou, A.; Doineau, R.; Briseno-Roa, L.; Canales-Herrerias, P.; Mary, P.; Rose, G.; Ortega, C.; Delincé, M.; Essono, S.; Jia, B.; Iannascoli, B.; Richard-Le Goff, O.; Kumar, R.; Stewart, S. N.; Pousse, Y.; Shen, B.; Grosselin, K.; Saudemont, B.; Sautel-Caillé, A.; Godina, A.; McNamara, S.; Eyer, K.; Millot, G. A.; Baudry, J.; England, P.; Nizak, C.; Jensen, A.; Griffiths, A. D.; Bruhns, P.; Brenan, C. *Nat. Biotechnol.* **2020**, *38*, 715−721.

(17) B Cell Memory and Plasma Cell Development. In *Molecular Biology of B Cells*; Elsevier, 2015; pp 227−249, Doi: DOI: 10.1016/B978-0-12-397933-9.00014-X.

(18) Wang, S.; Liu, Y.; Li, Y.; Lv, M.; Gao, K.; He, Y.; Wei, W.; Zhu, Y.; Dong, X.; Xu, X.; Li, Z.; Liu, L.; Liu, Y. *Anal. Chem.* **2022**, *94*, 918−926.

(19) Keating, S. M.; Mizrahi, R. A.; Adams, M. S.; Asensio, M. A.; Benzie, E.; Carter, K. P.; Chiang, Y.; Edgar, R. C.; Gautam, B. K.; Gras, A.; Leong, J.; Leong, R.; Lim, Y. W.; Manickam, V. A.; Medina-Cucurella, A. V.; Niedecken, A. R.; Saini, J.; Simons, J. F.; Spindler, M. J.; Stadtmiller, K.; Tinsley, B.; Wagner, E. K.; Wayham, N.; Tracy, L.; Lundberg, C. V.; Büscher, D.; Terencio, J. V.; Roalfe, L.; Pearce, E.; Richardson, H.; Goldblatt, D.; Ramjag, A. T.; Carrington, C. V. F.; Simmons, G.; Muench, M. O.; Chamow, S. M.; Monroe, B.; Olson, C.; Oguin, T. H.; Lynch, H.; Jeanfreau, R.; Mosher, R. A.; Walch, M. J.; Bartley, C. R.; Ross, C. A.; Meyer, E. H.; Adler, A. S.; Johnson, D. S. *Nat. Biotechnol.* **2021**, *39*, 989−999.

(20) Labisch, J. J.; Wiese, G. P.; Barnes, K.; Bollmann, F.; Pflanz, K. *PLoS One* **2021**, *16*, No. e0254739.

(21) Bounab, Y.; Eyer, K.; Dixneuf, S.; Rybczynska, M.; Chauvel, C.; Mistretta, M.; Tran, T.; Aymerich, N.; Chenon, G.; Llitjos, J.-F.; Venet, F.; Monneret, G.; Gillespie, I. A.; Cortez, P.; Moucadel, V.; Pachot, A.; Troesch, A.; Leissner, P.; Textoris, J.; Bibette, J.; Guyard, C.; Baudry, J.; Griffiths, A. D.; Védrine, C. *Nat. Protoc.* **2020**, *15*, 2920−2955.

(22) Stuart, T.; Butler, A.; Hoffman, P.; Hafemeister, C.; Papalexi, E.; Mauck, W. M.; Hao, Y.; Stoeckius, M.; Smibert, P.; Satija, R. *Cell* **2019**, *177*, 1888−1902.e21.

(23) Song, L.; Cohen, D.; Ouyang, Z.; Cao, Y.; Hu, X.; Liu, X. S. *Nat. Methods* **2021**, *18*, 627−630.

■ NOTE ADDED AFTER ASAP PUBLICATION

This paper was published ASAP on May 23, 2022. The Supporting Information was replaced, and the corrected version was reposted on May 24, 2022.

▭ Recommended by ACS

Targeted Intracellular Delivery of Trastuzumab Using Designer Phage Lambda Nanoparticles Alters Cellular Programs in Human Breast Cancer Cells

Alexis Catala, Carlos E. Catalano, *et al.*
JUNE 30, 2021
ACS NANO   READ ☑

Generation of Nanoyeast Single-Chain Variable Fragments as High-Avidity Biomaterials for Dengue Virus Detection

Fahimeh Farokhinejad, Matt Trau, *et al.*
NOVEMBER 05, 2021
ACS BIOMATERIALS SCIENCE & ENGINEERING   READ ☑

Cell-Permeant Bioadaptors for Cytosolic Delivery of Native Antibodies: A "Mix-and-Go" Approach

Shubo Du, Shao Q. Yao, *et al.*
NOVEMBER 26, 2020
ACS CENTRAL SCIENCE   READ ☑

Human Hexa-Histidine-Tagged Single-Chain Variable Fragments for Bioimaging of Bacterial Infections

Thae Thae Min and Montarop Yamabhai
DECEMBER 22, 2020
ACS OMEGA   READ ☑

Get More Suggestions >